

# IR nanospectroscopy mapping of facet-dependent sulfur poisoning and thermal regeneration on platinum nanocrystals

Lihi Rikanati, Yehonatan Hovav and Elad Gross \*

Received 1st December 2025, Accepted 16th January 2026

DOI: 10.1039/d5fd00139k

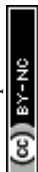
Sulfur poisoning critically limits the activity and durability of Pt catalysts, yet the nanoscale structure–reactivity relationships that govern sulfate adsorption and its thermal desorption remain poorly resolved. Using infrared nanospectroscopy, we directly map the spatial distribution, adsorption geometry, and temperature-dependent evolution of sulfate species on individual Pt nanocrystals (NCs) with well-defined facets. At room temperature, SO<sub>x</sub> species preferentially accumulate at defect-rich inter-facet regions, edges, and open Pt(100)-like facets, in which bidentate adsorption dominates. Flat Pt(111) terraces exhibit lower SO<sub>x</sub> coverage and a larger contribution from tridentate species. Mild annealing (50–200 °C) induces selective desorption from undercoordinated sites and drives a structural transition from bidentate to tridentate coordination as species migrate toward highly coordinated terrace regions. At 300 °C, most sulfate species desorb from edges and side facets, whereas thermally robust tridentate species persist at the NC interior. These results provide a facet-resolved picture of sulfur adsorption and regeneration pathways, revealing how local surface structure dictates the stability and thermal evolution of poisoning species on Pt catalysts.

## Introduction

Catalyst poisoning results in deactivation caused by the strong and often irreversible adsorption of molecular or atomic species to active metal sites.<sup>1</sup> Sulfur-containing compounds (*e.g.*, sulfuric acid and its derivatives), carbon monoxide, and halide ions are among the most potent poisoning agents.<sup>2,3</sup> The consequences of surface poisoning include reduced catalytic efficiency, lower product yields, and, ultimately, the need for catalyst replacement or regeneration.<sup>3–5</sup>

Poisons such as sulfur form strong bonds with Pt surface atoms, saturating active sites and preventing reactant adsorption. Chemical reactions between the poisoning species and the catalyst can also generate new surface compounds that

*Institute of Chemistry and The Center for Nanoscience and Nanotechnology, The Hebrew University, Jerusalem 91904, Israel. E-mail: elad.gross@mail.huji.ac.il*



may either desorb from the surface or further block catalytic sites.<sup>3</sup> Strongly bound poisons, such as  $\text{SO}_x$ -Pt species, often require harsh treatments for removal and restoration of catalytic activity.<sup>3,6-8</sup> Therefore, analyzing the adsorption and desorption patterns of  $\text{SO}_x$  species on Pt nanoparticles is essential for understanding the mechanisms of catalyst poisoning and guiding regeneration strategies.

The interaction between sulfuric acid and Pt depends strongly on the arrangement and coordination of the surface atoms and on the chemical properties of the  $\text{SO}_x$  species.<sup>9</sup> Sulfate is mainly adsorbed in bidentate or tridentate coordination modes and the adsorption geometry directly influences the adsorption strength and thermal stability of the poisoning species.<sup>10-12</sup> On Pt(111), sulfate predominantly adopts a well-ordered, bidentate or tridentate geometry stabilized by the close-packed terrace arrangement.<sup>13</sup> On Pt(100), which is characterized by a higher density of bridge sites, sulfate binds more weakly and often in a tilted bidentate configuration.<sup>14,15</sup>

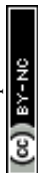
The natural inter- and intra-particle structural heterogeneity of catalytic nanoparticles<sup>16-20</sup> makes it challenging to directly probe how different surface sites influence  $\text{SO}_x$  poisoning and its removal. Resolving these site-dependent effects requires both experimental techniques capable of providing nanoscale chemical information and model catalysts with well-defined surface structures. Recent advances in high-spatial-resolution spectroscopy have enabled nanoscale investigations of catalytic nanoparticles,<sup>20-35</sup> and were also utilized for analysis of  $\text{SO}_x$  distributions on catalytic nanoparticles.<sup>7,36</sup> In particular, infrared nano-spectroscopy measurements<sup>37,38</sup> have shown that the types and adsorption geometries of  $\text{SO}_x$  species vary significantly due to morphological and structural heterogeneity among individual nanoparticles.<sup>7,36</sup> Using a similar approach, we have mapped the distribution and adsorption strength of surface ligands on Au nanocrystals with well-defined facets.<sup>39</sup>

In this work, we employ atomic force microscopy infrared (AFM-IR) measurements to map the distribution of  $\text{SO}_x$  species on Pt nanocrystals (NCs) with well-defined facets. We find that the majority of  $\text{SO}_x$  species adopt a bidentate adsorption mode and reside on the more open facets and at inter-facet regions, whereas only a minority of  $\text{SO}_x$  occupies the flat (111) facets. Annealing to 200 °C led to desorption from edge sites, accompanied by a transition from a bidentate adsorption mode to a tridentate adsorption mode. Further annealing to 300 °C led to desorption of most of the  $\text{SO}_x$  species, leaving residues near the center part of the nanocrystals, in which the  $\text{SO}_x$  is strongly adsorbed in a bidentate mode.

## Experimental

### Pt NCs preparation

A 15 nm-thick Pt film was e-beam evaporated onto a sapphire crystal (c-plane oriented, Gavish) using a glove-box evaporator (VST). Quartz crystal microbalance (QCM) measurements were used to assess the thickness of the evaporated film. NCs were prepared by annealing the Pt-coated sapphire at 1000 °C for 2 minutes under a nitrogen ( $\text{N}_2$ ) atmosphere. The sample was then immersed in 10 mM solution of  $\text{H}_2\text{SO}_4$  for 1 h at room temperature. Afterward, the sample was transferred to a vial on a hot plate pre-heated to 100 °C for 10 minutes in air in



order to remove physisorbed residues. Annealing of the sample was performed under a  $N_2$  atmosphere for 2 hours at the designated temperature.

### Nano-IR measurements

AFM-IR measurements were performed in tapping mode using a nanoIR-3 (Bruker) setup equipped with a Bruker Hyperspectral QCL laser source ( $790\text{--}1950\text{ cm}^{-1}$ ), gold-coated Si probes with a nominal diameter of  $\sim 25\text{ nm}$ , resonance frequencies of  $75 \pm 15\text{ kHz}$ , and spring constants of  $1\text{--}7\text{ N m}^{-1}$ . Averaged spectral acquisition time was 5 seconds per spectrum with a spectral resolution of  $2\text{ cm}^{-1}$ . The acquisition time was limited to 5 seconds to precisely define the measurement location and to prevent uncertainties caused by thermal drift.

### Focused ion beam (FIB) measurements

A dual-beam FIB instrument (FEI Helios) was employed for lamella extraction, and the resulting lamella was analyzed by high-resolution scanning-transmission electron microscopy (STEM) operated at 300 kV.

### X-ray photoelectron spectroscopy (XPS) measurements

Measurements were performed using a Kratos AXIS Supra spectrometer (Kratos Analytical) with an Al  $K\alpha$  monochromatic X-ray source ( $1486.6\text{ eV}$ ). The XPS spectra were acquired with a takeoff angle of  $90^\circ$  (normal to the analyzer), a pass energy of  $20\text{ eV}$  and a step size of  $0.1\text{ eV}$ ; the vacuum condition in the chamber was  $2 \times 10^{-9}\text{ Torr}$ . The binding energies were calibrated according to the C1s XPS peak position.

## Results and discussion

To identify the sensitivity of different atomic facets in Pt particles to sulfur poisoning, we focused our study on analyzing the adsorption and desorption of  $SO_x$  species on Pt nanocrystals (NCs) with well-defined Wulff-like structures. The NCs were prepared by annealing and then exposed to  $H_2SO_4$  to induce surface poisoning (see Experimental section for details), following recently published procedures.<sup>7,36</sup>

AFM topography images reveal NCs with lateral dimensions of  $200\text{--}400\text{ nm}$  and heights of up to  $100\text{ nm}$  (Fig. 1a). Exposure to  $H_2SO_4$  did not lead to noticeable morphological changes. Two main NC morphologies were observed: elongated, hexagon-like NCs with distinctly longer opposing sides, yielding a more rectangular appearance (highlighted with a yellow oval in Fig. 1a); and equilateral-like NCs resembling a rhombic structure (highlighted with a red oval in Fig. 1a).<sup>40</sup>

To identify the crystallographic facets of the NCs, a lamella was extracted from the sample using focused ion beam (FIB) milling, and transmission electron microscopy (TEM) images of both the hexagonal- and rhombic-like NCs were acquired (Fig. 1c and d, respectively), along with their corresponding electron diffraction patterns (insets, Fig. 1c and d). The hexagonal Pt nanocrystal exhibited a dominant (111) plane with adjacent (110) facets (Fig. 1c). The smaller rhombic NC displayed multiple crystallographic orientations, including prominent (111), (001), and (113) planes (Fig. 1d). The formation of these two distinct NC types is



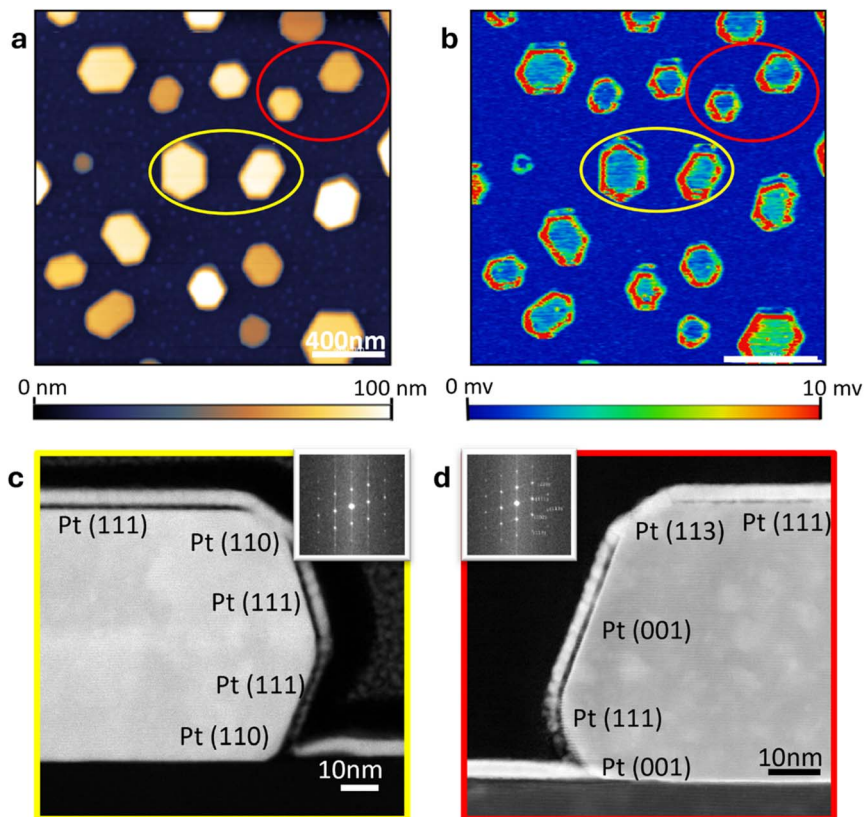


Fig. 1 Characterization of Pt NCs. (a) AFM topography image of Pt NCs following sulfur poisoning. Representative hexagon- and rhombic-like NCs are circled in yellow and red, respectively. (b) AFM-IR map at  $1100\text{ cm}^{-1}$ , acquired from the same area that was imaged by AFM. HR-TEM imaging of a cross-section of a hexagonal NC (c) and a rhombic NC (d), with their corresponding diffraction patterns (insets).

attributed to variations in local growth rates along different crystallographic directions, likely driven by subtle differences in the local defect density that influence facet stability. It is expected that these structural changes will impact the adsorption pattern of  $\text{SO}_x$ .<sup>41–46</sup>

AFM-IR mapping was performed at  $1100\text{ cm}^{-1}$  (Fig. 1b), which corresponds to the S–O vibration of the sulfate anion,<sup>47</sup> on the same area imaged by AFM (Fig. 1a). The IR signal intensity varied across the NCs, with higher signals detected at edges, steps, and the more open facets, while weaker signals appeared on the inner, flat (111) facets. These variations provide evidence for facet-dependent adsorption behavior and show the dominant role of nanocrystal structure in governing the local surface density of  $\text{SO}_x$  species.

Single NC analyses, including localized IR spectral measurements and AFM-IR mapping, were conducted to obtain high-resolution, sub-particle information on  $\text{SO}_x$  adsorption, distribution, and desorption (Fig. 2). An AFM topography image of a hexagon-like NC is shown in Fig. 2a(i). IR spectra were acquired at the edge and the center of the NC (the measurement positions are indicated by red and



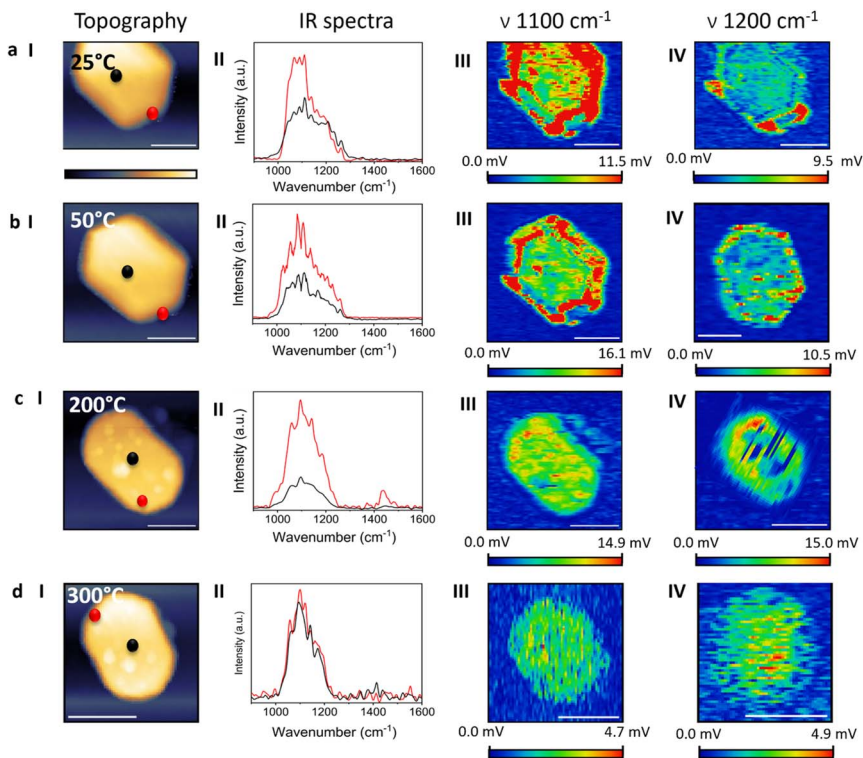


Fig. 2 AFM-IR analysis of hexagonal NC. AFM topography (i), localized IR spectra (ii), and AFM-IR mapping at  $1100\text{ cm}^{-1}$  (iii) and  $1200\text{ cm}^{-1}$  (iv), following surface poisoning by  $\text{H}_2\text{SO}_4$ . Measurements were conducted at room temperature (a(i)–a(iv)), after annealing to  $50\text{ }^\circ\text{C}$  (b(i)–b(iv)),  $200\text{ }^\circ\text{C}$  (c(i)–c(iv)) and  $300\text{ }^\circ\text{C}$  (d(i)–d(iv)). AFM topography images are shown in a(i), b(i), c(i) and d(i). IR spectra were acquired from the center (black spectrum) and edge (red spectrum) of a Pt NC and are shown in a(ii), b(ii), c(ii) and d(ii). The locations from which the IR measurements were acquired are indicated by black and red circles in the AFM topography images. The ratio between the red and black spectra reflects differences in signal intensities at different surface sites. Spectra shown in the different panels were normalized according to the amplitude of the red spectra. The AFM images following annealing were acquired in different areas of the sample, and therefore different NCs were analyzed following each thermal treatment. Scale bar represents  $200\text{ nm}$ .

black dots in Fig. 2a(i)), and are presented as red and black spectra, respectively, in Fig. 2a(ii). The spectra exhibit a broad feature spanning  $1000\text{--}1280\text{ cm}^{-1}$ . The spectrum acquired at the center of the NC shows a stronger contribution in the  $1000\text{--}1100\text{ cm}^{-1}$  region.

Sulfuric acid adsorbs on Pt primarily through bidentate and tridentate binding modes.<sup>7,48,49</sup> The bidentate (2-fold) adsorption mode is energetically favored at undercoordinated sites such as edges, steps, and defects.<sup>44,50–53</sup> Tridentate (3-fold) adsorption occurs when the sulfate species coordinates with three adjacent Pt atoms, a geometry that is mostly realized on atomically flat, close-packed terraces.<sup>7,11,36</sup> It was demonstrated that sulfate adsorbs on Pt(100) and Pt(110) in a 2-fold geometry ( $C_{2v}$  symmetry) and induces two IR bands around  $1100$  and  $1200\text{ cm}^{-1}$ , assigned to the stretching vibration of the S–O bond in  $\text{SO}_4^{2-}$



coordinated to Pt atoms and that of the uncoordinated S–O bond, respectively. Sulfate adsorption on Pt(111) gives a single IR band at around  $1200\text{ cm}^{-1}$ , which is assigned to the S–O stretching vibration of a 3-fold adsorption geometry.<sup>47</sup>

The spectrum measured at the edge of the NC showed a higher signal at  $\sim 1100\text{ cm}^{-1}$ , which correlated to a dominant presence of sulfuric acid with a bidentate adsorption geometry on this site (red spectrum, Fig. 2a(ii)). The IR signal that was acquired at the center of the NC showed a similar amplitude at the  $1000\text{--}1250\text{ cm}^{-1}$  range, indicative that both bidentate and tridentate binding modes of sulfuric acid coexist on these sites (black spectrum, Fig. 2a(ii)).

AFM-IR maps were acquired at  $1100$  and  $1200\text{ cm}^{-1}$  (Fig. 2a(iii) and (iv), respectively) to identify the spatial distribution of bidentate and tridentate adsorption modes across the facets of the NCs. The IR map at  $1100\text{ cm}^{-1}$  (Fig. 2a(iii)) shows strong signal intensities at the nanocrystal edges and on the side Pt(110) facets, with reduced intensity at the NC center. AFM-IR mapping at  $1200\text{ cm}^{-1}$  (Fig. 2a(iv)) exhibits weaker signals that are primarily localized at inter-facet regions and edge sites. The IR mapping supports the results shown in the localized IR spectra and shows that there is a preference toward a 2-fold adsorption geometry at sites with low-coordinated surface atoms.

Integration of the IR mapping and spectroscopy data reveals that the surface structure of Pt NCs governs the surface distribution of  $\text{SO}_x$ . The spectral signature associated with the 2-fold (bidentate) adsorption mode of sulfate ( $\sim 1100\text{ cm}^{-1}$ ) was detected across most regions of the NCs, with high signal variability across the NC. Higher signal intensity was observed on the side facets and at inter-facet regions, whereas lower intensity appeared on the flat Pt(111) terraces. The spectral signature corresponding to the 3-fold (tridentate) adsorption mode ( $\sim 1200\text{ cm}^{-1}$ ) was weaker, and was characterized by local enhancement at inter-facet regions and the more open (110) facets.

To obtain a quantitative measure of the spatial distribution of  $\text{SO}_x$  species, the NC was segmented into concentric rings at increasing radial distances from its center. The IR signal amplitude within each ring was averaged and the averaged IR intensities—analyzed from the IR maps at  $1100$  and  $1200\text{ cm}^{-1}$ —were plotted

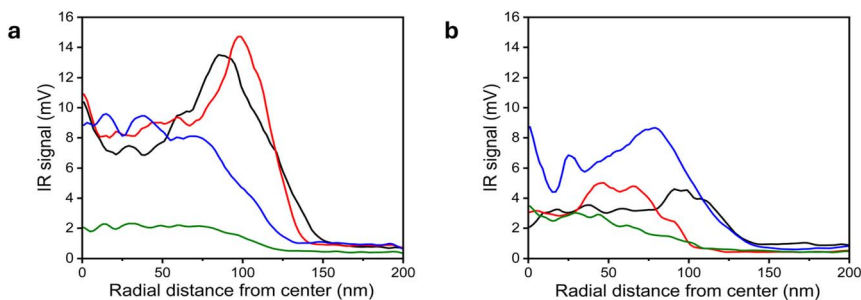
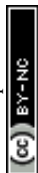


Fig. 3 Quantitative analysis of AFM-IR maps. The AFM-IR maps shown in Fig. 2 were analyzed by dividing each nanocrystal into concentric rings originating from its center. The AFM-IR signal within each ring was extracted and averaged to obtain the mean intensities at  $1100\text{ cm}^{-1}$  (a) and  $1200\text{ cm}^{-1}$  (b) as a function of the radial distance of the ring from the nanocrystal center. This analysis was performed for IR maps that were acquired at room temperature (black curves), and after annealing at  $50\text{ }^\circ\text{C}$  (red curves),  $200\text{ }^\circ\text{C}$  (blue curves) and  $300\text{ }^\circ\text{C}$  (green curves).



as a function of the radial distance of each concentric ring from the NC center (Fig. 3a and b, respectively). This analysis revealed a detectable spectral contribution at the NC center for the IR signal at  $1100\text{ cm}^{-1}$  (black curve, Fig. 3a) and a pronounced  $\sim 50\%$  enhancement in the IR intensity at a radial distance of approximately 75 nm, corresponding to inter-facet regions where  $\text{SO}_x$  species preferentially accumulate. Quantitative analysis of the IR mapping at  $1200\text{ cm}^{-1}$  (black curve, Fig. 3b) showed a lower and much more homogeneous signal, with a relatively small increase at the particle's rim. These results show that the distribution of  $\text{SO}_x$  species in the tridentate binding mode is more consistent on the NC surface, in comparison to the dominant bidentate mode that was mainly observed at inter-facets and side facets.

Analysis of the IR signal at room temperature reveals a clear preference for  $\text{SO}_x$  adsorption in a bidentate adsorption mode on edge sites and on more open facets. The bidentate mode was consistently more prominent than the tridentate mode, and more heterogeneous in its dispersion on the NC surface. This indicates competitive adsorption at identical surface sites, with the energetically less demanding bidentate configuration dominating under ambient conditions.

IR maps and localized IR spectra were acquired following annealing at  $50\text{ }^\circ\text{C}$  (Fig. 2b). The localized IR spectra showed lower intensity in the high-wavenumber contribution, resulting in a more pronounced peak near  $1100\text{ cm}^{-1}$  (Fig. 2b(ii)). The IR map at  $1100\text{ cm}^{-1}$  (Fig. 2b(iii)) showed a decrease in the overall signal intensity and a stronger localization at inter-facet regions. Averaged analysis of the IR signal revealed enhanced localization of the  $1100\text{ cm}^{-1}$  signal at inter-facet regions (Fig. 3a, red curve). The IR map at  $1200\text{ cm}^{-1}$  (Fig. 2b(iv)) exhibited a more spatially dispersed signal after annealing, with some preference for inter-facet sites, as also identified in the quantitative analysis (Fig. 3b, red curve). These results indicate that mild annealing promotes localization of bidentate species on inter-facet sites, which contain higher densities of surface defects, whereas tridentate species diffuse inward toward flatter regions, which facilitates the 3-fold binding geometry.

This trend was enhanced following annealing at  $200\text{ }^\circ\text{C}$  (Fig. 2c). After annealing, the IR spectrum exhibited a dominant peak at  $1100\text{ cm}^{-1}$  with a substantially diminished  $1200\text{ cm}^{-1}$  contribution (Fig. 2c(ii)). The peak at  $1420\text{ cm}^{-1}$ , which was detected in the IR spectra acquired at edge sites, is attributed to carboxylate species that were formed on the NC surface following exposure of organic residues to high temperature. IR mapping at  $1100\text{ cm}^{-1}$  showed a lower signal intensity at inter-facet sites, and the signal amplitude at the NC center became comparable to the one measured at the edges, as also indicated in the quantitative analysis (Fig. 3a, blue curve). In contrast, AFM-IR mapping at  $1200\text{ cm}^{-1}$  showed an overall increase in signal intensity and specifically at edge sites (Fig. 2c(iv)), consistent with the averaged IR analysis (Fig. 3b, blue curve). These findings suggest that annealing at  $200\text{ }^\circ\text{C}$  promotes a transition from a bidentate adsorption mode to a tridentate adsorption mode, enabled by the added thermal energy required to activate this transition.

Further annealing at  $300\text{ }^\circ\text{C}$  led to sharpening and localization of the IR peak to the  $1020\text{--}1220\text{ cm}^{-1}$  region at both the center and the edge of the NC (Fig. 2d(ii)), and the spectral amplitudes at these locations became comparable, indicative of desorption from edge sites. IR mapping at  $1100\text{ cm}^{-1}$  (Fig. 2d(iii)) showed a pronounced decrease in signal intensity across the NC (Fig. 3a, green



curve), with the averaged value in the interior region lower by  $\sim 80\%$  compared to the signal measured at room temperature.

IR mapping at  $1200\text{ cm}^{-1}$  showed a reduced signal at the outer regions of the NC, yet significant intensity persisted at the NC interior even after annealing at  $300\text{ }^\circ\text{C}$  (Fig. 2d(iv) and Fig. 3b, green curve). These results indicate that after annealing at  $300\text{ }^\circ\text{C}$ ,  $\text{SO}_x$  species are no longer detected at inter-facet sites, whereas tridentate is the favored configuration on the interior part of the NC. This highlights the higher thermal stability of  $\text{SO}_x$  species bound in a tridentate mode to flat, highly coordinated regions compared to the more reactive edge sites.

A similar temperature-dependent analysis was conducted for a more symmetric NC (Fig. 4a(i)). IR spectra were acquired at the edge and center of the NC and displayed a broad IR band spanning  $1000\text{--}1300\text{ cm}^{-1}$ , with a stronger

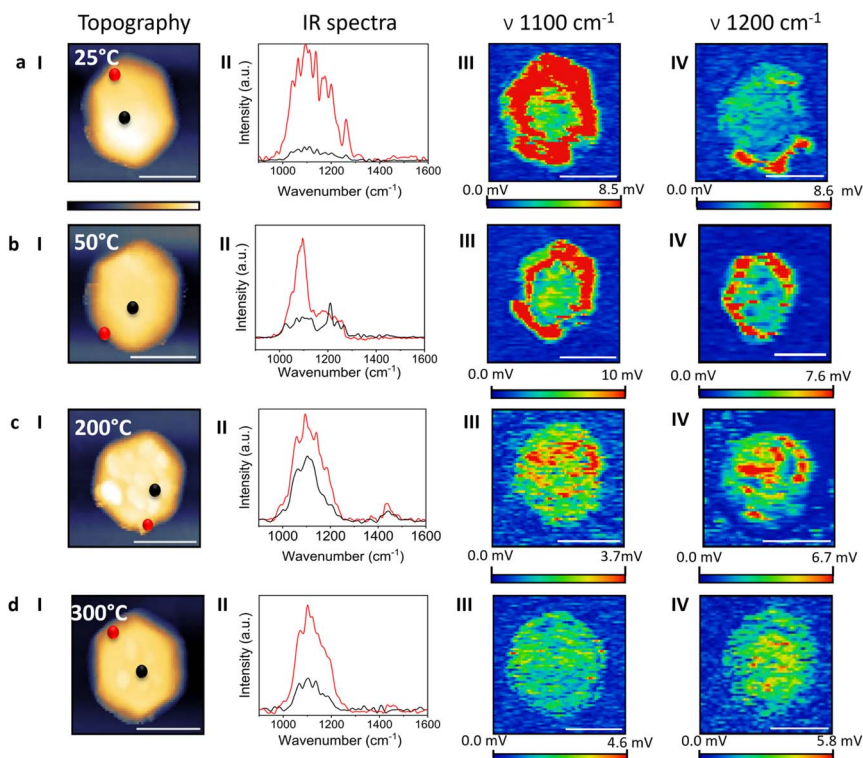


Fig. 4 AFM-IR mapping of a single NC. AFM topography (i), localized IR spectra (ii), and AFM-IR mapping at  $1100\text{ cm}^{-1}$  (iii) and  $1200\text{ cm}^{-1}$  (iv), following surface poisoning by  $\text{H}_2\text{SO}_4$ . Measurements were conducted at room temperature (a(i)–a(iv)), after annealing at  $50\text{ }^\circ\text{C}$  (b(i)–b(iv)),  $200\text{ }^\circ\text{C}$  (c(i)–c(iv)) and  $300\text{ }^\circ\text{C}$  (d(i)–d(iv)). AFM topography images are shown in a(i), b(i), c(i) and d(i). IR spectra were acquired from the center (black spectrum) and edge (red spectrum) of a Pt NC and are shown in a(ii), b(ii), c(ii) and d(ii). The locations in which the IR measurements were acquired are indicated by black and red circles in the AFM topography images. The ratio between the red and black spectra reflects differences in the signal intensities at different surface sites. All spectra shown in the different panels were normalized according to the amplitude of the red spectra. The AFM images following annealing were acquired from different areas of the sample, and therefore different NCs were analyzed following each thermal treatment. Scale bar represents  $200\text{ nm}$ .



signal at the edge of the NC (Fig. 4a(ii)). IR mapping at  $1100\text{ cm}^{-1}$  revealed a pronounced signal on the side facets and inter-facet regions (Fig. 4a(iii)), whereas the  $1200\text{ cm}^{-1}$  feature appeared weaker and spatially confined (Fig. 4a(iv)). In both cases, the IR intensity was highest on the side facets and lower on the flat (111) facet, consistent with the quantitative IR mapping analysis (Fig. 5, black curves). The dominant signal at  $1100\text{ cm}^{-1}$  indicates the preference toward a bidentate adsorption geometry, which is further enhanced on side facets.

Annealing at  $50\text{ }^{\circ}\text{C}$  led to a lower amplitude in the  $1200\text{--}1300\text{ cm}^{-1}$  range for the spectra measured at the side of the NC (red spectrum, Fig. 4b(ii)), while sharper and more distinct contributions in the  $1200\text{--}1300\text{ cm}^{-1}$  region were probed in the spectra measured at the center of the NC (black spectrum, Fig. 4b(ii)). Correspondingly, the IR maps showed lower overall signal intensities and more localized features (Fig. 4b(iii) and (iv)), consistent with desorption from edge sites, as also validated by the quantitative IR analysis (Fig. 5, red curves).

Further annealing at  $200\text{ }^{\circ}\text{C}$  resulted in an additional decrease in the  $1200\text{--}1300\text{ cm}^{-1}$  range (Fig. 4c(ii)). The improved signal-to-noise ratio observed in the black spectrum in panel c(ii) is attributed to a local increase in the surface density of the adsorbed species, which also results in a relatively higher signal compared to other spectra that were acquired at the center of the NCs. The IR map at  $1100\text{ cm}^{-1}$  showed a substantial reduction in signal intensity across the NC (Fig. 4c(iii)), and the quantitative analysis (Fig. 5a, blue curve) confirmed a major overall decrease. The IR map at  $1200\text{ cm}^{-1}$  revealed a lower overall signal amplitude (Fig. 4c(iv)), verified by quantitative analysis (Fig. 5b, blue curve). Thus, annealing at  $200\text{ }^{\circ}\text{C}$  promoted desorption, and specifically desorption from edge sites.

Local IR spectra were measured after annealing at  $300\text{ }^{\circ}\text{C}$  and showed a stronger signal at the edges of the NC (Fig. 4d(ii)). IR maps (Fig. 4d(iii) and (iv)) and their quantitative analysis (Fig. 5a, green curve) revealed that annealing at  $300\text{ }^{\circ}\text{C}$  led to a minor decrease in the averaged  $1100\text{ cm}^{-1}$  intensity. The  $1200\text{ cm}^{-1}$  signal at the center of the NC increased following annealing (Fig. 5b,

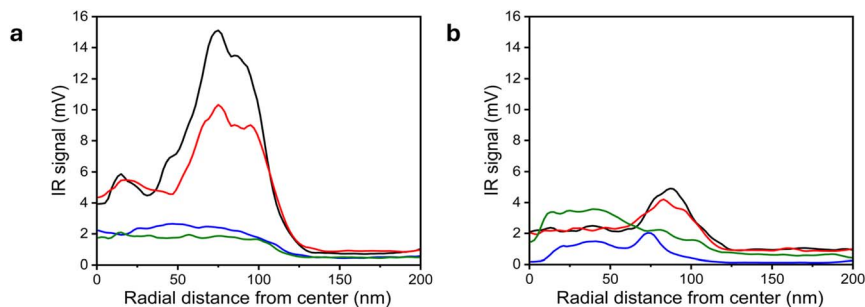


Fig. 5 Quantitative analysis of AFM-IR. The AFM-IR maps shown in Fig. 4 were analyzed by dividing each nanocrystal into concentric rings originating from its center. The AFM-IR signal within each ring was extracted and averaged to obtain the mean intensities at  $1100\text{ cm}^{-1}$  (a) and  $1200\text{ cm}^{-1}$  (b) as a function of the radial distance of the ring from the nanocrystal center. This analysis was performed for IR maps that were acquired at room temperature (black curves), and after annealing at  $50\text{ }^{\circ}\text{C}$  (red curves),  $200\text{ }^{\circ}\text{C}$  (blue curves) and  $300\text{ }^{\circ}\text{C}$  (green curves).



green curve), indicating diffusion of the tridentate species to the central region of the NC and transformation from a bidentate adsorption mode to a tridentate adsorption mode.

Integration of the nanoscale measurements demonstrates clear temperature-dependent changes in both the surface density and adsorption mode of  $\text{SO}_x$  species. At room temperature,  $\text{SO}_x$  adsorption is nonuniform, with higher coverage at defect-rich inter-facet and side-facet regions, and a preference for the bidentate adsorption mode. Annealing at 200 °C results in selective desorption from edge sites and a shift from bidentate to tridentate adsorption at the NC interior. This trend becomes more pronounced after annealing at 300 °C, where  $\text{SO}_x$  species persist primarily at the NC center and show a preference toward the tridentate adsorption mode.

Temperature-dependent S2p X-ray photoelectron spectra (XPS) were acquired to complement the nanospectroscopy analysis (Fig. 6). At room temperature, the XP spectrum (red spectrum, Fig. 6) showed a strong peak at 169.0 eV, characteristic of  $\text{S}^{6+}$  in sulfate species, along with contributions from  $\text{S}^{4+}$  in  $\text{SO}_2$ -related species. Following annealing at 50 °C (blue spectrum, Fig. 6), the 169.0 eV peak showed a decrease in intensity, consistent with partial desorption, along with a broader peak profile, indicating the coexistence of various  $\text{SO}_x$  species adsorbed in different adsorption geometries.

Following annealing at 200 °C (green spectrum, Fig. 6), the peak centered at 169.0 eV was narrowed and a new signal was detected at 163.0 eV, which correlated to sulfur in lower oxidation states ( $\text{S}^0$ ,  $\text{S}^{1-}$ , or  $\text{S}^{2-}$ ). This likely follows a sequence of surface-mediated reduction steps, consistent with previous studies,<sup>54-56</sup> and marks the onset of thermal reduction, followed by desorption. Further annealing at 300 °C (orange spectrum, Fig. 6) leads to a substantial

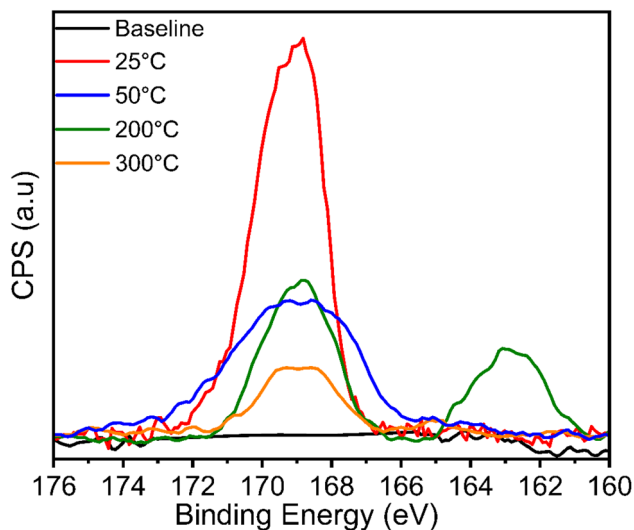


Fig. 6 S2p XPS spectra of Pt NCs before (black spectrum) and after their exposure  $\text{H}_2\text{SO}_4$ . XPS measurements of the poisoned NCs were acquired at room temperature (red spectrum), and after annealing at 50 °C (blue spectrum), 200 °C (green spectrum) and 300 °C (orange spectrum).



decrease in signal amplitude. This result highlights the thermal desorption of SO<sub>x</sub> species from the surface of Pt NCs at relatively moderate temperatures.<sup>57,58</sup> The fact that these transformations occur under an N<sub>2</sub> environment further confirms that Pt NCs catalyze the selective reduction and removal of surface-bound SO<sub>x</sub> through thermal activation, which is facilitated on sites that are characterized by a high density of surface defects.

## Conclusions

AFM-IR nanospectroscopy measurements reveal that sulfate adsorption on Pt NCs is strongly governed by local coordination and facet structure. Defect-rich edges, steps, and inter-facet regions serve as high-affinity sites that predominantly stabilize bidentate sulfate, whereas flat Pt(111)-like terraces exhibit lower overall coverage and a stronger tendency toward tridentate coordination. Temperature-dependent measurements show that annealing triggers selective desorption from undercoordinated sites and promotes diffusion of sulfate species into terrace regions, where the transition from bidentate to tridentate adsorption becomes thermodynamically favored. Upon annealing at 300 °C, most SO<sub>x</sub> species detach from edge sites, leaving behind a small population of thermally persistent tridentate species bound to terrace atoms. These findings, which were supported by XPS measurements, establish a direct correlation between facet geometry, adsorption mode, and thermal stability of SO<sub>x</sub> species, offering fundamental insights into site-dependent poisoning and regeneration processes in Pt-based catalysts.

## Author contributions

The manuscript was written through contributions of all authors. All authors have given approval to the final version of the manuscript. Conceptualization, methodology and data curation: LR and EG; formal analysis: YH and EG; writing—original draft: LR; writing—review & editing: EG; supervision: EG.

## Conflicts of interest

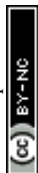
There are no conflicts to declare.

## Data availability

The datasets supporting this article, titled “IR nanospectroscopy mapping of facet-dependent sulfur poisoning and thermal regeneration on platinum nanocrystals”, are openly available on Zenodo and can be accessed via <https://doi.org/10.5281/zenodo.17778202>.

## Acknowledgements

This research was supported by the Israel Science Foundation grant (Grant Agreement No. 2118/22). The authors acknowledge Dr Sergei Remennik (Hebrew University Center for Nanoscience and Nanotechnology) for conducting HR-TEM and diffraction measurements.



## References

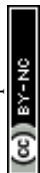
- 1 M. D. Argyle and C. H. Bartholomew, Heterogeneous Catalyst Deactivation and Regeneration: A Review, *Catalysts*, 2015, **5**, 145–269, DOI: [10.3390/catal5010145](https://doi.org/10.3390/catal5010145).
- 2 B. J. Hare, R. A. Garcia Carcamo, L. L. Daemen, Y. Cheng, R. B. Getman and C. Sievers, Poisoning of Pt/ $\gamma$ -Al<sub>2</sub>O<sub>3</sub> Aqueous Phase Reforming Catalysts by Ketone and Diketone-Derived Surface Species, *ACS Catal.*, 2024, **14**(3), 1480–1493, DOI: [10.1021/acscatal.3c04774](https://doi.org/10.1021/acscatal.3c04774).
- 3 W. Chen, J. Cao, W. Fu, J. Zhang, G. Qian, J. Yang, D. Chen, X. Zhou, W. Yuan and X. Duan, Molecular-Level Insights into the Notorious CO Poisoning of Platinum Catalyst, *Angew. Chem., Int. Ed.*, 2022, **61**(16), e202200190, DOI: [10.1002/anie.202200190](https://doi.org/10.1002/anie.202200190).
- 4 K. J. Kim, Y. L. Lee, G. R. Hong, S. Y. Ahn, B. J. Kim, S. S. Lee, Y. Jeon and H. S. Roh, A Study on the Activity Recovery Behavior of Noble Metal Catalysts against Sulfur Poisoning, *Catal. Today*, 2024, **425**, 114361, DOI: [10.1016/j.cattod.2023.114361](https://doi.org/10.1016/j.cattod.2023.114361).
- 5 S. Liu, T. Wang, X. Wu, J. Li, S. Liu and R. Ran, Sulfur Poisoning and Thermal Regeneration of Silica-Alumina Supported Platinum Catalyst for Soot Oxidation, *Surf. Interfaces*, 2025, **68**, 106732, DOI: [10.1016/j.surfin.2025.106732](https://doi.org/10.1016/j.surfin.2025.106732).
- 6 M. I. Awad, M. M. Saleh and T. Ohsaka, Impact of SO<sub>2</sub> Poisoning of Platinum Nanoparticles Modified Glassy Carbon Electrode on Oxygen Reduction, *J. Power Sources*, 2011, **196**(8), 3722–3728, DOI: [10.1016/j.jpowsour.2010.12.080](https://doi.org/10.1016/j.jpowsour.2010.12.080).
- 7 Z. Say, M. Kaya, Ç. Kaderoğlu, Y. Koçak, K. E. Ercan, A. T. Sika-Nartey, A. Jalal, A. A. Turk, C. Langhammer, M. Jahangirzadeh Varjovi, E. Durgun and E. Ozensoy, Unraveling Molecular Fingerprints of Catalytic Sulfur Poisoning at the Nanometer Scale with Near-Field Infrared Spectroscopy, *J. Am. Chem. Soc.*, 2022, **144**(19), 8848–8860, DOI: [10.1021/jacs.2c03088](https://doi.org/10.1021/jacs.2c03088).
- 8 M. S. Wilburn and W. S. Epling, Formation and Decomposition of Sulfite and Sulfate Species on Pt/Pd Catalysts: An SO<sub>2</sub> Oxidation and Sulfur Exposure Study, *ACS Catal.*, 2019, **9**(1), 640–648, DOI: [10.1021/acscatal.8b03529](https://doi.org/10.1021/acscatal.8b03529).
- 9 L. F. Gaudin, M. Kang and C. L. Bentley, Facet-Dependent Electrocatalysis and Surface Electrochemical Processes on Polycrystalline Platinum, *Electrochim. Acta*, 2023, **450**, 142223, DOI: [10.1016/j.electacta.2023.142223](https://doi.org/10.1016/j.electacta.2023.142223).
- 10 M. J. Ungerer, C. G. C. E. van Sittert and N. H. de Leeuw, Behavior of S, SO, and SO<sub>3</sub> on Pt (001), (011), and (111) Surfaces: A DFT Study, *J. Chem. Phys.*, 2021, **154**(19), 194701, DOI: [10.1063/5.0043501](https://doi.org/10.1063/5.0043501).
- 11 N. Hoshi, A. Sakurada, S. Nakamura, S. Teruya, O. Koga and Y. Hori, Infrared Reflection Absorption Spectroscopy of Sulfuric Acid Anion Adsorbed on Stepped Surfaces of Platinum Single-Crystal Electrodes, *J. Phys. Chem. B*, 2002, **106**(8), 1985–1990, DOI: [10.1021/jp012456o](https://doi.org/10.1021/jp012456o).
- 12 J. Mostany, E. Herrero, J. M. Feliu and J. Lipkowski, Thermodynamic Studies of Anion Adsorption at Stepped Platinum(hkl) Electrode Surfaces in Sulfuric Acid Solutions, *J. Phys. Chem. B*, 2002, **106**(49), 12787–12796, DOI: [10.1021/jp026561p](https://doi.org/10.1021/jp026561p).
- 13 M. Aoki, T. Shishido, T. Morooka, T. Nakanishi and T. Masuda, Electrochemical Oxidative Desorption of Adsorbed Sulfur Species on (111)



- Surfaces of Single Crystals of Pure Pt and Pt-Based Bimetallic Alloys, *J. Phys. Chem. C*, 2025, **129**(4), 2122–2131, DOI: [10.1021/acs.jpcc.4c06652](https://doi.org/10.1021/acs.jpcc.4c06652).
- 14 M. J. Hossain, M. M. Rahman and M. Jafar Sharif, Preference for Low-Coordination Sites by Adsorbed CO on Small Platinum Nanoparticles, *Nanoscale Adv.*, 2020, **2**(3), 1245–1252, DOI: [10.1039/c9na00499h](https://doi.org/10.1039/c9na00499h).
- 15 C. K. Rhee, B. J. Kim, C. Ham, Y. J. Kim, K. Song and K. Kwon, Size Effect of Pt Nanoparticle on Catalytic Activity in Oxidation of Methanol and Formic Acid: Comparison to Pt(111), Pt(100), and Polycrystalline Pt Electrodes, *Langmuir*, 2009, **25**(12), 7140–7147, DOI: [10.1021/la900204c](https://doi.org/10.1021/la900204c).
- 16 J. Van Loon, A. V. Kubarev and M. B. J. Roeffaers, Correlating Catalyst Structure and Activity at the Nanoscale, *ChemNanoMat*, 2018, **4**, 6–14, DOI: [10.1002/cnma.201700301](https://doi.org/10.1002/cnma.201700301).
- 17 I. M. N. Groot, Investigation of Active Catalysts at Work, *Acc. Chem. Res.*, 2021, **54**(23), 4334–4341, DOI: [10.1021/acs.accounts.1c00429](https://doi.org/10.1021/acs.accounts.1c00429).
- 18 J. I. J. Choi, T. S. Kim, D. Kim, S. W. Lee and J. Y. Park, *Operando* Surface Characterization on Catalytic and Energy Materials from Single Crystals to Nanoparticles, *ACS Nano*, 2020, **14**, 16392–16413, DOI: [10.1021/acsnano.0c07549](https://doi.org/10.1021/acsnano.0c07549).
- 19 W. Xu, J. S. Kong, Y. T. E. Yeh and P. Chen, Single-Molecule Nanocatalysis Reveals Heterogeneous Reaction Pathways and Catalytic dynamics, *Nat. Mater.*, 2008, **7**(12), 992–996, DOI: [10.1038/nmat2319](https://doi.org/10.1038/nmat2319).
- 20 M. B. J. Roeffaers, G. De Cremer, J. Libeert, R. Ameloot, P. Dedecker, A. J. Bons, M. Bückins, J. A. Martens, B. F. Sels, D. E. De Vos and J. Hofkens, Super-Resolution Reactivity Mapping of Nanostructured Catalyst Particles, *Angew. Chem., Int. Ed.*, 2009, **48**(49), 9285–9289, DOI: [10.1002/anie.200904944](https://doi.org/10.1002/anie.200904944).
- 21 S. Dery, B. Friedman, H. Shema and E. Gross, Mechanistic Insights Gained by High Spatial Resolution Reactivity Mapping of Homogeneous and Heterogeneous (Electro)Catalysts, *Chem. Rev.*, 2023, **123**, 6003–6038, DOI: [10.1021/acs.chemrev.2c00867](https://doi.org/10.1021/acs.chemrev.2c00867).
- 22 L. Rikanati, S. Dery and E. Gross, AFM-IR and s-SNOM-IR Measurements of Chemically Addressable Monolayers on Au Nanoparticles, *J. Chem. Phys.*, 2021, **155**(20), 204704, DOI: [10.1063/5.0072079](https://doi.org/10.1063/5.0072079).
- 23 X. Mao, C. Liu, M. Hesari, N. Zou and P. Chen, Super-Resolution Imaging of Non-Fluorescent Reactions via Competition, *Nat. Chem.*, 2019, **11**(8), 687–694, DOI: [10.1038/s41557-019-0288-8](https://doi.org/10.1038/s41557-019-0288-8).
- 24 C. Y. Wu, W. J. Wolf, Y. Levartovsky, H. A. Bechtel, M. C. Martin, F. D. Toste and E. Gross, High-Spatial-Resolution Mapping of Catalytic Reactions on Single Particles, *Nature*, 2017, **541**(7638), 511–515, DOI: [10.1038/nature20795](https://doi.org/10.1038/nature20795).
- 25 S. Dery, H. Mehlman, L. Hale, M. Carmiel-Kostan, R. Yemini, T. Ben-Tzvi, M. Noked, F. D. Toste and E. Gross, Site-Independent Hydrogenation Reactions on Oxide-Supported Au Nanoparticles Facilitated by Intraparticle Hydrogen Atom Diffusion, *ACS Catal.*, 2021, **11**(15), 9875–9884, DOI: [10.1021/acscatal.1c01987](https://doi.org/10.1021/acscatal.1c01987).
- 26 Z. Li and D. Kourouski, Plasmon-Driven Chemistry on Mono- And Bimetallic Nanostructures, *Acc. Chem. Res.*, 2021, **54**(10), 2477–2487, DOI: [10.1021/acs.accounts.1c00093](https://doi.org/10.1021/acs.accounts.1c00093).
- 27 B. Friedman, L. Giloni, O. M. Gazit and E. Gross, Nanoscale Chemical Imaging of Basic Sites Distribution on Catalytically Active Mg–Al Mixed Oxide Particles, *Chem. Biomed. Imaging*, 2025, **3**(8), 560–568, DOI: [10.1021/cbmi.5c00017](https://doi.org/10.1021/cbmi.5c00017).



- 28 M. A. Karreman, I. L. C. Buurmans, J. W. Geus, A. V. Agronskaia, J. Ruiz-Martínez, H. C. Gerritsen and B. M. Weckhuysen, Integrated Laser and Electron Microscopy Correlates Structure of Fluid Catalytic Cracking Particles to Brønsted Acidity, *Angew. Chem., Int. Ed.*, 2012, **51**(6), 1428–1431, DOI: [10.1002/anie.201106651](https://doi.org/10.1002/anie.201106651).
- 29 S. Dery, S. Kim, D. Feferman, H. Mehlman, F. D. Toste and E. Gross, Site-Dependent Selectivity in Oxidation Reactions on Single Pt Nanoparticles, *Phys. Chem. Chem. Phys.*, 2020, **22**(34), 18765–18769, DOI: [10.1039/d0cp00642d](https://doi.org/10.1039/d0cp00642d).
- 30 S. Dery, S. Kim, D. Haddad, A. Cossaro, A. Verdini, L. Floreano, F. D. Toste and E. Gross, Identifying Site-Dependent Reactivity in Oxidation Reactions on Single Pt Particles, *Chem. Sci.*, 2018, **9**(31), 6523–6531, DOI: [10.1039/c8sc01956h](https://doi.org/10.1039/c8sc01956h).
- 31 J. Ruiz-Martínez, A. M. Beale, U. Deka, M. G. O'Brien, P. D. Quinn, J. F. W. Mosselmanns and B. M. Weckhuysen, Correlating Metal Poisoning with Zeolite Deactivation in an Individual Catalyst Particle by Chemical and Phase-Sensitive X-Ray Microscopy, *Angew. Chem., Int. Ed.*, 2013, **52**(23), 5983–5987, DOI: [10.1002/anie.201210030](https://doi.org/10.1002/anie.201210030).
- 32 M. H. F. Kox, K. F. Domke, J. P. R. Day, G. Rago, E. Stavitski, M. Bonn and B. M. Weckhuysen, Label-Free Chemical Imaging of Catalytic Solids by Coherent Anti-Stokes Raman Scattering and Synchrotron-Based Infrared Microscopy, *Angew. Chem., Int. Ed.*, 2009, **48**(47), 8990–8994, DOI: [10.1002/anie.200904282](https://doi.org/10.1002/anie.200904282).
- 33 O. M. Busch, W. Brijoux, S. Thomson and F. Schüth, Spatially Resolving Infrared Spectroscopy for Parallelized Characterization of Acid Sites of Catalysts via Pyridine Sorption: Possibilities and Limitations, *J. Catal.*, 2004, **222**(1), 174–179, DOI: [10.1016/j.jcat.2003.11.002](https://doi.org/10.1016/j.jcat.2003.11.002).
- 34 G. De Cremer, E. Bartholomeeusen, P. P. Pescarmona, K. Lin, D. E. De Vos, J. Hofkens, M. B. J. Roeffiaers and B. F. Sels, The Influence of Diffusion Phenomena on Catalysis: A Study at the Single Particle Level Using Fluorescence Microscopy, *Catal. Today*, 2010, **157**, 236–242, DOI: [10.1016/j.cattod.2010.04.035](https://doi.org/10.1016/j.cattod.2010.04.035).
- 35 J. A. Bergwerff, T. Visser, B. R. G. Leliveld, B. D. Rossenaar, K. P. De Jong and B. M. Weckhuysen, Envisaging the Physicochemical Processes during the Preparation of Supported Catalysts: Raman Microscopy on the Impregnation of Mo onto Al<sub>2</sub>O<sub>3</sub> Extrudates, *J. Am. Chem. Soc.*, 2004, **126**(44), 14548–14556, DOI: [10.1021/ja040107c](https://doi.org/10.1021/ja040107c).
- 36 M. Kostan-Carmiel, A. Theodoridis, H. R. Eisenberg, T. Stein, C. Langhammer and E. Gross, Nanoscale Analysis of Sulfur Poisoning Effects on Hydrogen Sorption in Single Pd Nanoparticles, *ACS Nano*, 2025, **19**(42), 36969–36981, DOI: [10.1021/acsnano.5c08917](https://doi.org/10.1021/acsnano.5c08917).
- 37 A. Dazzi and C. B. Prater, AFM-IR: Technology and Applications in Nanoscale Infrared Spectroscopy and Chemical Imaging, *Chem. Rev.*, 2017, 5146–5173, DOI: [10.1021/acs.chemrev.6b00448](https://doi.org/10.1021/acs.chemrev.6b00448).
- 38 D. Kourouski, A. Dazzi, R. Zenobi and A. Centrone, Infrared and Raman Chemical Imaging and Spectroscopy at the Nanoscale, *Chem. Soc. Rev.*, 2020, 3315–3347, DOI: [10.1039/c8cs00916c](https://doi.org/10.1039/c8cs00916c).
- 39 L. Rikanati, H. Shema, T. Ben-Tzvi and E. Gross, Nanoimaging of Facet-Dependent Adsorption, Diffusion, and Reactivity of Surface Ligands on Au



- Nanocrystals, *Nano Lett.*, 2023, 23(12), 5437–5444, DOI: [10.1021/acs.nanolett.3c00250](https://doi.org/10.1021/acs.nanolett.3c00250).
- 40 B. Zhang, D. Wang, Y. Hou, S. Yang, X. H. Yang, J. H. Zhong, J. Liu, H. F. Wang, P. Hu, H. J. Zhao and H. G. Yang, Facet-Dependent Catalytic Activity of Platinum Nanocrystals for Triiodide Reduction in Dye-Sensitized Solar Cells, *Sci. Rep.*, 2013, 3, 1836, DOI: [10.1038/srep01836](https://doi.org/10.1038/srep01836).
- 41 P. Wongbua-ngam, W. Veerasai, P. Wilairat and O. U. Kheowan, Model Interpretation of Electrochemical Behavior of Pt/H<sub>2</sub>SO<sub>4</sub> Interface over Both the Hydrogen Oxidation and Oxide Formation Regions, *Int. J. Hydrogen Energy*, 2019, 44(23), 12108–12117, DOI: [10.1016/j.ijhydene.2019.03.076](https://doi.org/10.1016/j.ijhydene.2019.03.076).
- 42 M. H. Huang, S. Rej and S. C. Hsu, Facet-Dependent Properties of Polyhedral Nanocrystals, *Chem. Commun.*, 2014, 50(14), 1634–1644, DOI: [10.1039/c3cc48527g](https://doi.org/10.1039/c3cc48527g).
- 43 B. C. Han, C. R. Miranda and G. Ceder, Effect of Particle Size and Surface Structure on Adsorption of O and OH on Platinum Nanoparticles: A First-Principles Study, *Phys. Rev. B:Condens. Matter Mater. Phys.*, 2008, 77(7), 075410, DOI: [10.1103/PhysRevB.77.075410](https://doi.org/10.1103/PhysRevB.77.075410).
- 44 N. Hoshi, M. Kuroda, T. Ogawa, O. Koga and Y. Hori, Infrared Reflection Absorption Spectroscopy of the Sulfuric Acid Anion Adsorbed on Pd(S)-[n(111) × (111)] Electrodes, *Langmuir*, 2004, 20(12), 5066–5070, DOI: [10.1021/la036149g](https://doi.org/10.1021/la036149g).
- 45 X. M. Zeng, R. Huang, G. F. Shao, Y. H. Wen and S. G. Sun, High-Index-Faceted Platinum Nanoparticles: Insights into Structural and Thermal Stabilities and Shape Evolution from Atomistic Simulations, *J. Mater. Chem. A*, 2014, 2(29), 11480–11489, DOI: [10.1039/c4ta01731e](https://doi.org/10.1039/c4ta01731e).
- 46 V. Mastronardi, E. Magliocca, J. S. Gullon, R. Brescia, P. P. Pompa, T. S. Miller and M. U. Moglianetti, Coating-Free, Pyramidal Platinum Nanoparticles for High Stability Fuel Cell Oxygen Reduction, *ACS Appl. Mater. Interfaces*, 2022, 14(32), 36570–36581, DOI: [10.1021/acsami.2c07738](https://doi.org/10.1021/acsami.2c07738).
- 47 N. Hoshi, A. Sakurada, S. Nakamura, S. Teruya, O. Koga and Y. Hori, Infrared Reflection Absorption Spectroscopy of Sulfuric Acid Anion Adsorbed on Stepped Surfaces of Platinum Single-Crystal Electrodes, *J. Phys. Chem. B*, 2002, 106(8), 1985–1990, DOI: [10.1021/jp012456o](https://doi.org/10.1021/jp012456o).
- 48 I. Y. Zhang, G. Zwaschka, Z. Wang, M. Wolf, R. K. Campen and Y. Tong, Resolving the Chemical Identity of H<sub>2</sub>SO<sub>4</sub> Derived Anions on Pt(111) Electrodes: They're Sulfate, *Phys. Chem. Chem. Phys.*, 2019, 21(35), 19147–19152, DOI: [10.1039/c9cp03397a](https://doi.org/10.1039/c9cp03397a).
- 49 F. Gossenberger, F. Juarez and A. Groß, Sulfate, Bisulfate, and Hydrogen Co-Adsorption on Pt(111) and Au(111) in an Electrochemical Environment, *Front. Chem.*, 2020, 8, 634, DOI: [10.3389/fchem.2020.00634](https://doi.org/10.3389/fchem.2020.00634).
- 50 E. Groppo, S. Rojas-Buzo and S. Bordiga, The Role of In Situ/Operando IR Spectroscopy in Unraveling Adsorbate-Induced Structural Changes in Heterogeneous Catalysis, *Chem. Rev.*, 2023, 12135–12169, DOI: [10.1021/acs.chemrev.3c00372](https://doi.org/10.1021/acs.chemrev.3c00372).
- 51 Y. Xia, D. Nelli, R. Ferrando, J. Yuan and Z. Y. Li, Shape Control of Size-Selected Naked Platinum Nanocrystals, *Nat. Commun.*, 2021, 12(1), 3019, DOI: [10.1038/s41467-021-23305-7](https://doi.org/10.1038/s41467-021-23305-7).



- 52 H. Lee, S. E. Habas, S. Kweskin, D. Butcher, G. A. Somorjai and P. Yang, Morphological Control of Catalytically Active Platinum Nanocrystals, *Angew. Chem., Int. Ed.*, 2006, **45**(46), 7824–7828, DOI: [10.1002/anie.200603068](https://doi.org/10.1002/anie.200603068).
- 53 K. Y. Yeh, N. A. Restaino, M. R. Esopi, J. K. Maranas and M. J. Janik, The Adsorption of Bisulfate and Sulfate Anions over a Pt(1 1 1) Electrode: A First Principle Study of Adsorption Configurations, Vibrational Frequencies and Linear Sweep Voltammogram Simulations, *Catal. Today*, 2013, **202**(1), 20–35, DOI: [10.1016/j.cattod.2012.03.011](https://doi.org/10.1016/j.cattod.2012.03.011).
- 54 C. H. Chen, A. Halford, M. Walker, C. Brennan, S. C. S. Lai, D. J. Fermin, P. R. Unwin and P. Rodriguez, Electrochemical Characterization and Regeneration of Sulfur Poisoned Pt Catalysts in Aqueous Media, *J. Electroanal. Chem.*, 2018, **816**, 138–148, DOI: [10.1016/j.jelechem.2018.03.015](https://doi.org/10.1016/j.jelechem.2018.03.015).
- 55 M. Y. Smirnov, A. V. Kalinkin, A. V. Pashis, I. P. Prosvirin and V. I. Bukhtiyarov, Interaction of SO<sub>2</sub> with Pt Model Supported Catalysts Studied by XPS, *J. Phys. Chem. C*, 2014, **118**(38), 22120–22135, DOI: [10.1021/jp5069126](https://doi.org/10.1021/jp5069126).
- 56 M. Aoki, T. Shishido, T. Morooka, T. Nakanishi and T. Masuda, Electrochemical Oxidative Desorption of Adsorbed Sulfur Species on (111) Surfaces of Single Crystals of Pure Pt and Pt-Based Bimetallic Alloys, *J. Phys. Chem. C*, 2025, **129**(4), 2122–2131, DOI: [10.1021/acs.jpcc.4c06652](https://doi.org/10.1021/acs.jpcc.4c06652).
- 57 A. F. Lee and K. Wilson, Sulfate-Enhanced Catalytic Destruction of 1,1,1-Trichloroethane over Pt(111), *J. Phys. Chem. B*, 2006, **110**(2), 907–913, DOI: [10.1021/jp054658g](https://doi.org/10.1021/jp054658g).
- 58 C. H. Chen, A. Halford, M. Walker, C. Brennan, S. C. S. Lai, D. J. Fermin, P. R. Unwin and P. Rodriguez, Electrochemical Characterization and Regeneration of Sulfur Poisoned Pt Catalysts in Aqueous Media, *J. Electroanal. Chem.*, 2018, **816**, 138–148, DOI: [10.1016/j.jelechem.2018.03.015](https://doi.org/10.1016/j.jelechem.2018.03.015).

